Supplementary Information (SI) for Catalysis Science & Technology.

Experimental and computational optimisation of methanol dehydration to dimethyl ether

Maciej G. Walerowski,[a] Stylianos Kyrimis,[b] Matthew E. Potter,[c] Alice E. Oakley,[a] Marina Carravetta,[a] Lindsay-Marie Armstrong,[b] and Robert Raja[a]

[a] School of Chemistry and Chemical Engineering, University of Southampton, Southampton, SO17 1BJ, UK.
[b] School of Engineering, University of Southampton, Southampton, SO17 1BJ, UK.
[c] Department of Chemistry, University of Bath, Bath, BA2 7AY, UK.

1 Synthesis protocols

1.1 Large scale SAPO-11

A large batch of SAPO-11 for studying the influence of temperature, catalyst granule size, catalyst bed length and reactant gas stream methanol concentration on the MTD reaction was synthesised as follows, by adapting an approach outlined by Murthy *et al.*[1] Deionised water (70 mL, GPR Rectapur 1.0 µs/cm, VWR Chemicals) was added to a 1 L Teflon beaker. Aluminium isopropoxide (58.35 g, >98%, Sigma-Aldrich) was slowly added to the beaker under mixing and stirred at 700 rpm for 15 minutes. In a separate glass beaker, deionised water (56 mL, 18.2 MΩ) and phosphoric acid (32.29 g, >85 wt% in H_2O, Sigma-Aldrich) were mixed. The aqueous phosphoric acid solution was then slowly added to the aluminium solution and stirred at 700 rpm for 60 minutes. Dipropylamine (28.33 g, 99%, Sigma-Aldrich) was then slowly added dropwise to the Teflon beaker and stirred for further 120 minutes at 700 rpm. Ludox AS-40 (8.42 g, 40 wt% suspension in water, Sigma-Aldrich) then added dropwise to the Teflon beaker and mixed for further 180 minutes at 700 rpm. The uniform white gel of ratio 1:0Al:1.0P:0.2Si:1.0DPA:25H_2O was then crystallised in a Teflon lined Parr batch reactor at 200°C for 48 hours with no mixing. Once crystallisation was complete, the Parr reactor was immediately quenched in ice and the white solid separated via centrifugation. The white solid was then washed twice with water and any unreacted/amorphous material was separated via sedimentation and skimming. Crystalline material was dried overnight at 70°C and then calcined at 600°C for 40 hours in flowing air with a 2.5°C/min ramp rate to yield a fine, white crystalline material.

1.2 SAPO-11 catalysts with different Si loading

Four SAPO-11 catalysts with target Si/Al ratios of either 0.05, 0.10, 0.15 or 0.20 for studying the influence of BAS abundance on the MTD reaction were synthesised by modifying a method outlined by Grenev *et al.*[2] Deionised water (18.02 g, GPR Rectapur 1.0 µs/cm, VWR Chemicals) was added to a 250 mL Teflon beaker. Phosphoric acid (4.62 g, >85 wt% in H_2O, Sigma-Aldrich) added to the beaker and mixed at 350 rpm for 10 minutes. Aluminium isopropoxide (8.34 g, , >98%, Sigma-Aldrich) slowly added to the beaker under stirring and stirred at 500 rpm for 90 minutes. Dipropylamine (2.05 g, 99%, Sigma-Aldrich) added dropwise to the beaker and stirred at 500 rpm for 120 minutes. Ludox AS-40 (0.31, 0.65, 0.92 or 1.22 g, 40 wt% suspension in water, Sigma-Aldrich) then added dropwise and stirred at 500 rpm for 150 minutes. The uniform white gel of ratio 1:0Al:1.0P:0.05-0.20Si:0.5DPA:25H_2O was then crystallised in Teflon lined stainless steel autoclaves at 200°C for 24 hours with no mixing. Once crystallisation was complete, the autoclaves were immediately quenched in ice and the white solid separated via centrifugation. The white solid was then washed twice with water and any unreacted/amorphous material was separated via sedimentation and skimming. Crystalline material was dried overnight at 70°C and then calcined at 600°C for 40 hours in flowing air with a 2.5°C/min ramp rate to yield a fine, white crystalline material.

2 Characterisation protocols

2.1 Energy Dispersive Spectroscopy (EDS)

EDS analysis was performed using an Oxford Instruments EDS (backscattered electron – composition (BED-C)) detector which was integrated into a JSM-7200F field emission scanning electron microscope. AZtect software was used for elemental analysis. Powder was loaded directly onto a carbon tape and analysed without any sputter coating. 10 kV acceleration voltage was used with a working distance between 8 and 12 mm. For EDS elemental composition, 2 separate particle-rich regions were selected, in each image, 5 particle zones were scanned. Each particle region was around 100-1000 µm in size which resulted in analysis of a high number of particles. Elemental composition was obtained by averaging those 10 separate scans and the error shows the standard deviation between the scans.

2.2 Powder X-ray diffraction (XRD)

PXRD characterisation was performed using a Bruker D2 Phaser instrument. Patterns were obtained using Cu Kα radiation (λ = 1.54184 Å) at 30 kV voltage and 10 mA current using a 0.6 mm slit. Patterns were obtained in the 5-45° 2θ range with 0.01° increments and 0.4 s per step. Whole powder pattern fitting (WPPF) was performed using Rigaku PDXL 2 software to obtain the unit cell parameters. LaB_6 was used as the width standard. CIF file for the AEL framework was obtained from the IZA database of zeolite structures.[3]

2.3 Surface area and porosity

Surface area and porosity characterisation was performed using Micromeritics Tristar II 3020 analyser. N_2 was used as the adsorptive, and a liquid N_2 bath was utilised. Analysis performed between 0.00 and 0.95 p/p_0 (relative pressure). 124 adsorption and 30 desorption points were used to obtain the full physisorption isotherm. BET surface area and pore volume were calculated automatically by the Micromeritics Tristar II 3020 software. Samples (~0.15 g) were thoroughly degassed prior to measurements for a minimum of 21 hours using a Micrometrics Vac Prep 062 system by heating them under vacuum at 120°C, with final pressure of ~100 mTorr.

2.4 Scanning Electron Microscopy (SEM)

Scanning electron microscopy (SEM) characterisation was performed using a JEOL JSM-7200F field emission scanning electron microscope. 5 kV acceleration voltage was used with 93 µA emission current. Working distance ranged between 6 and 12 mm. Sample was imaged directly on tape without prior sputter coating.

2.5 Solid state nuclear magnetic resonance (ssNMR)

For all ssNMR analysis, the samples were thoroughly dried overnight at 180°C under a Schlenk line vacuum. The samples were then transferred under a nitrogen atmosphere into a glovebox. All ssNMR rotors were packed under a nitrogen atmosphere in a glovebox to minimise exposure to moisture. Post-processing of NMR data was done using MestreNova software.

For the ^{27}Al and ^{31}P analysis, the weighed samples (~0.03 g) were packed into a 3.2 mm thin wall zirconium rotor. Analysis was performed using an Agilent Varian 600 MHz Premium Shielded spectrometer, with a 14.1 T field strength. OpenVnmrJ software was utilised. The rotors were span at 14,000 Hz at the magic angle and the spectra acquired in triple (^{1}H-^{27}Al-^{31}P) resonance mode. The ^{27}Al spectra were acquired at 156.46 MHz using a 312500 Hz spectral width, 20 ms acquisition time, 3 s recycle delay, 128 scans, 63 W power, 2000 aX90 amplitude and 1.2 µs pwX90 pulse width. The ^{31}P spectra were acquired at 243.06 MHz using 100000 Hz spectral width, 20 ms acquisition time, 25 s recycle delay, 128 scans, 63 W power, 3800 aX90 amplitude and 3.25 µs pwX90 pulse width. YAG and H_3PO_4 standards were used to calibrate the ^{27}Al and ^{31}P chemical shift axes, respectively.

For the ^{29}Si analysis, the weighed samples (~0.08 g) were packed into a 4 mm zirconium rotor and capped with a KELF rotor/cap. Analysis was performed using a Bruker 600 MHz wide bore Ultrashield spectrometer, with a 14.1 T field strength. Topspin 4.0.7 software was utilised. The rotors were span at 8000 Hz at the magic angle and the spectra acquired in double (^{1}H-^{29}Si) resonance mode. The ^{29}Si spectra were acquired in direct acquisition mode. Direct acquisition spectra were acquired with proton decoupling, 4 µs pulse width, 200 W power, 10 W decoupling power, 260 scans and 300 s relaxation delay. TMSS standard was used to calibrate the ^{29}Si chemical shift axis.

2.6 Ammonia Temperature Programmed Desorption (NH3-TPD)

NH_3-TPD experiments were performed on Quantachrome ChemBET Pulsar TPR/TPD instrument. 0.2 g of 100 – 425 µm pelletised sample was dried at 550°C for 2 hours under a 24 mL/min He and 6 mL/min O_2 flow. Sample was then cooled down to 150°C and put under a 30 mL/min flow of 5% NH_3/He, the sample was held at 150°C for 2 hours. Flow was then changed to 30 mL/min He and sample held at 150°C for further 2 hours. System was then heated to 600°C at a rate of 5°C/min and evolution of NH_3 as a function of temperature was monitored. The system was then held at 600°C for 1 hour to fully desorb any remaining NH_3.

2.7 Carbon Hydrogen Nitrogen (CHN)

CHN analysis was performed by the London Metropolitan University elemental analysis service. The samples were weighed using a Mettler Toledo high precision scale and analysed using a ThermoFlash 2000. Samples analysed in duplicate and the error shows the standard deviation between the two results.

3 Catalytic protocol

Catalysis was performed in a custom built reactor which comprised of a nitrogen cylinder, mass flow and temperature controller, dual syringe pump, heating jacket, round bottom flask and a round bottom flask heater. A similar reactor set-up was used previously to study ethanol dehydration over solid acid catalysts, such as SAPO-34.[4–6]

The SAPO-11 catalysts powders were pelletised at 4 tonnes for 10 s to obtain self-supporting pellets of 2.5 cm diameter which were then crushed and sieved 5 times to obtain catalyst granules in either a 106-300, 300-500 or 500-710 µm range. The catalyst granules (0.150, 0.300 or 0.450 g) were then loaded into a 40 cm quartz reactor tube (0.4 cm i.d, 0.6 cm o.d) and sandwiched between two layers of 1 mm borosilicate beads. Bottom borosilicate bead layer was adjusted to ensure the catalyst bed was located in the isothermal zone of the reactor. The top borosilicate bead layer length was kept constant for all catalysts to ensure reproducible mixing and heating of the reaction gas.

Catalysts were activated at 400°C in a 25 mL/min flow of nitrogen for 1 hour before the reaction. The reactor was then cooled to 170°C before methanol (3, 6, 12 or 18 µL/min, equivalent to WHSV of 0.5, 1, 2 or 3 h^{-1} for 0.300 g of catalyst, respectively) was passed into the reactor along with a 25 (or 31, 38 or 41 for WHSV experiments) mL/min stream of nitrogen. The nitrogen flow rate was adjusted so that the total vapour flow (methanol and nitrogen) was constant, despite the variation in methanol flow rate. The outlet from the reactor was mixed with a 3, 6, 12, or 18 µL/min flow of chloroform, which served as the external standard. The reactor outlet, mixed with the chloroform standard, was continuously flown into a 250 mL round bottom flask, which was heated to 120°C to prevent condensation. 0.2 mL samples were taken from this flask for manual injection into the Perkin Elmer Clarus 480 gas chromatograph (GC) for analysis.

The injector of the GC was set at 170°C, and the injection was carried in a He carrier gas through an Elite-5 column (5% diphenyl/95% dimethyl polysiloxane, 30m, 0.25 mm, 0.25 µm), within a 30°C isothermal oven. The hydrocarbon species were quantified using a flame ionisation detector set at 250°C with a total analysis time of 5 minutes. Outlet gas was analysed in triplicate, reactor temperature was then increased by 15°C and the process repeated. Each experiment was performed in triplicate, using fresh catalyst on a different day in a randomised order. Standard deviation was calculated between the repeat results and presented as an error bar.

Mass balances (accounting for both methanol and dimethyl ether) were calculated using the chloroform external standard, using GC response factors, experimentally determined by our own calibrations. In all cases the mass balances were found to be between 95 and 105 mol%, as expected.

For the time-on-stream stability study, the temperature and methanol WHSV were held at 275°C and 3 h^{-1} throughout the study to accelerate catalyst deactivation.

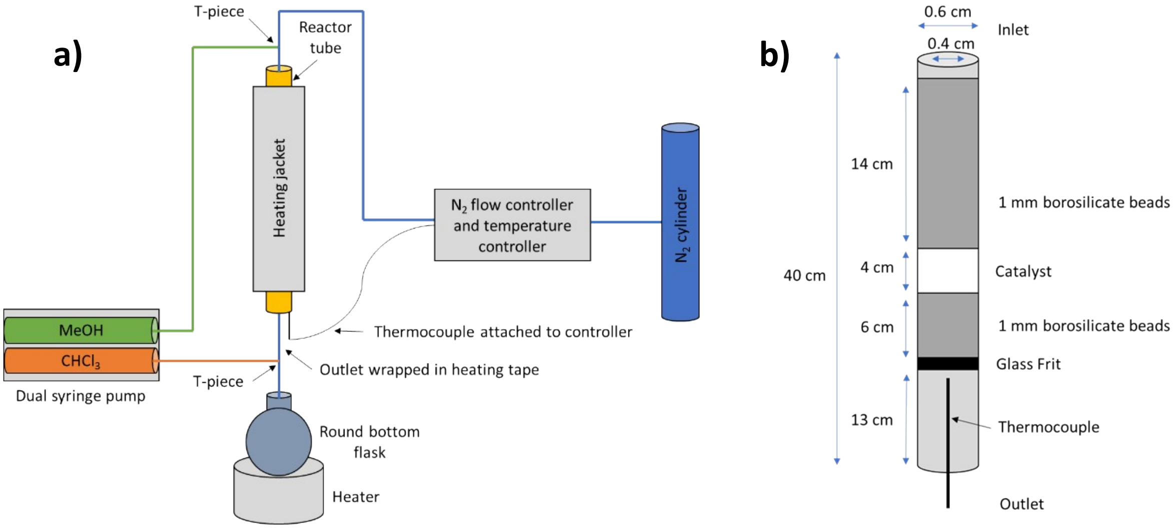

Fig. S1 Schematic of **a)** reactor system and **b)** reactor tube used for methanol dehydration over SAPO-11 catalysts.

To determine the combined gaseous flow rate of methanol and nitrogen, the gaseous methanol flow rate was firstly calculated. This was estimated by considering the volumetric expansion of methanol during evaporation as outlined in equation S1. The combined gaseous flow rate could then be calculated by summing the individual methanol and nitrogen gas flow rates.

Equation S1
$$\frac{Methanol\ Density\ at\ 27^{\circ}C\ and\ 1\ bar}{Methanol\ Density\ at\ 227^{\circ}C\ and\ 1\ bar}\ x\ Methanol\ Liquid\ Flow\ Rate$$

For a methanol WHSV of 3 h^{-1}, the combined gaseous flow of methanol and nitrogen could thus be estimated as shown in Equation S2. Combined gas flow rate and hence residence time can thus be kept similar by increasing the nitrogen flow rate to counteract the decrease in methanol gas flow rate as the methanol WHSV is reduced.

Equation S2
$$\left(\frac{784.5\ kg\ m^{-3}}{0.774\ kg\ m^{-3}}\ x\ 0.01896\ mL\ min^{-1}\right) + 25\ mL\ min^{-1} = 44.2\ mL\ min^{-1}$$

4 Kinetic model set-up

Methanol dehydration over SAPO-11 was modelled using a first-order rate equation (Equation S3 and S4).

Equation S3
$$Rate = k[MeOH]$$

Equation S4
$$k = Ae^{-\frac{Ea}{RT}}$$

Where *Rate* is the rate of reaction (mol cm^{-3} s^{-1}), *k* is the reaction rate coefficient (s^{-1}), *[MeOH]* is the concentration of methanol in mol cm^{-3}, *A* is the pre-exponential factor (s^{-1}), *Ea* is the activation energy for the reaction (J mol^{-1}), *R* is the universal gas constant (J mol^{-1} K^{-1}) and *T* is the temperature (K).

The experimentally observed rate constant *k,* was estimated at a range of temperatures using the open source software Copasi.[7] A genetic algorithm with a population size of 2000 and 100 generations was used for the initial estimation of *k*,[8] followed by a Levenberg-Marquardt local optimisation to obtain the final value of *k*.[9,10] Equation S4 can be rearranged into its non-exponential form as shown in Equation S5. The apparent activation energy and pre-exponential factor for methanol dehydration over SAPO-11 was then calculated from the gradient and intercept of the linear plot obtained by plotting *ln(k)* vs *1/T*. The average activation energy and pre-exponential factor was calculated by averaging the individual values for the four different methanol WHSVs considered.

Equation S5
$$ln(k) = ln(A) - \frac{Ea}{RT}$$

5 Computational fluid dynamics (CFD) model set-up

A three-dimensional CFD model was built in Ansys Fluent 19.2.[11] Only the catalytic bed was modelled as it was experimentally confirmed that the borosilicate bead layers are chemically unreactive. Catalyst bed was modelled using a cylindrical geometry (0.2 cm radius and a 1.9, 3.6, or 5.4 cm height) and meshed using Ansys meshing to give 700,000 hexahedral computational cells. Thermal equilibrium between solid and fluid phases was assumed. Inlet, wall, and outlet initial temperatures were set to match experimental temperatures and the wall was defined as a non-slip boundary. Pressure across the model was set to atmospheric to match experimental conditions. Inlet was defined as a mass flow inlet with mass fractions defined from the respective WHSV. A k-ω turbulence model was applied with a term introduced in the diffusion model to account for turbulent viscosity. A SIMPLE scheme was used for pressure-velocity coupling with second-order upwind equations used for hydrodynamic terms and for the species scalars.[12] The following under relaxation values were used: 0.7 for pressure, 0.3 for momentum and energy and 0.5 for scalars. Simulation proceeded for 4000 iterations or until convergence was reached whichever came first. The residuals were: 5×10^{-4} for all scalars, momentum and continuity, 1×10^{-6} for energy, and 1×10^{-3} for k-ω.

Capabilities of the model were extended using user defined functions in which additional parameters were included to replicate the physiochemical phenomena more accurately. Dusty-gas diffusion model was used to describe diffusion through the catalyst bed as per Kyrimis *et al.*[13] Particles were assumed to be homogenous and spherical with an average diameter of 200 µm. Inertial and viscous resistances were calculated from the Ergun equation.[14] Porosity across the bed was modelled using de Klerk's correlation.[15] Full description and derivation of associated conservation equations used for CFD modelling can be found in Kyrimis *et al.*[16]

Methanol dehydration over SAPO-11 was modelled using a modified Arrhenius equation which took into account limited active site number as shown in Equations S6-S8.

$$k = \frac{Ae^{\frac{-Ea}{RT}}}{\left(\frac{A_{cat}}{V_{cat}}\right)^2 Z_k}$$

Equation S6

Where A_{cat} is the surface area of the catalyst, V_{cat} is the volume of the catalyst and Z_k is the active site surface coverage, with its influence described in Equations S7 and S8.

$$if\ [MeOH] > [Si]\ then\ \frac{1}{Z_k} = \frac{[Si]}{[MeOH]}$$

Equation S7

$$if\ [Si] \geq [MeOH] then\ \frac{1}{Z_k} = 1$$

Equation S8

Eq. S7 and S8 describe that if the local concentration of MeOH is greater than the local number of Si active sites, then the overall rate of the reaction will be limited by the number of Si sites. This is sensible as when all Si sites are occupied, the catalyst is fully utilised and any MeOH beyond that will be unreactive. On the contrary, if the local concentration of MeOH is lower than the Si sites, MeOH concentration will determine the magnitude of Z_k.

Not all Si will generate catalytically active Brønsted acid sites in SAPO-11 as some may form inactive Si islands. Using the correlation between Si loading and Si island formation developed by Grenev *et al.*,[2] based on a 2.7 wt% Si loading for this SAPO-11 catalyst, only 61% of this Si will be catalytically active. This is then considered when calculating the number of active sites [Si].

6 Design of Experiment

A three-factorial DoE study employing a single centre point was employed to investigate the influence of reaction temperature (245-275°C), catalyst bed length (2.5-7.5 cm) and methanol WHSV (4-6 h^{-1}) on simulated methanol conversion over SAPO-11. On top of the 8 vertex and 1 centre point cases, 6 additional cases inside the design space were investigated to give 15 unique points. The 15 individual cases were simulated using the CFD model described in section 5 and the results processed using the Sartorius MODDE® 13.1 Pro software suite.[17] The results were fitted using a MLR model to give a model with an R^2 of 0.88 and RSD of 7%.

7 Characterisation results

7.1 Large scale SAPO-11 catalyst

Phase purity of SAPO-11(2.7) was confirmed as the observed XRD pattern matched well the simulated pattern for an AEL framework (Fig. S2).[3] Calculated unit cell parameters (Table S2) were in agreement with those for an idealised AEL unit cell.[3] A type IV N_2 physisorption isotherm (Fig. S3a) was obtained which is in line with published results for SAPO-11.[1,18] The pore size distribution plot (Fig. S3b) indicates a lack of ordered mesopores within the framework, with the H4 hysteresis loop suggesting that the observed hysteresis is due to interparticle voids.[19] BET surface area of 124 m^2g^{-1} and pore volume of 0.09 cm^3g^{-1} (Table S3) is within the range reported for other SAPO-11 samples.[1,18,20–22] SEM demonstrated that SAPO-11(2.7) particles of ~10 µm possess spheroidal shape and are composed of smaller crystallites (Fig. S4) which is typical of SAPO-11.[18,20,22,23]

Table S1 Elemental composition of SAPO-11(2.7) determined using EDS.

Aluminium (wt%)	Phosphorous (wt%)	Silicon (wt%)
20.1 ± 0.5	20.6 ± 0.7	2.7 ± 0.2

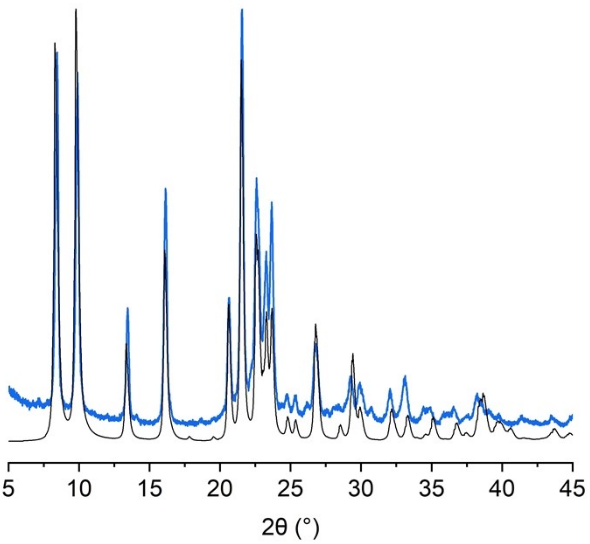

Fig. S2 Powder XRD pattern of dried SAPO-11(2.7) (blue) compared to calculated AEL pattern (black) confirming phase purity.

Table S2 Unit cell parameters obtained via WPFF of SAPO-11(2.7) showing minor variation compared to an ideal AEL unit cell. Error in lattice parameter estimation is ± 0.03 Å.

Catalyst	a (Å)	b (Å)	c (Å)	α (°)	β (°)	γ (°)	Volume (Å^3)
Ideal AEL	8.31	18.73	13.39	90.00	90.00	90.00	2085
SAPO-11(2.7)	8.31	18.30	13.39	90.00	90.00	90.00	2037

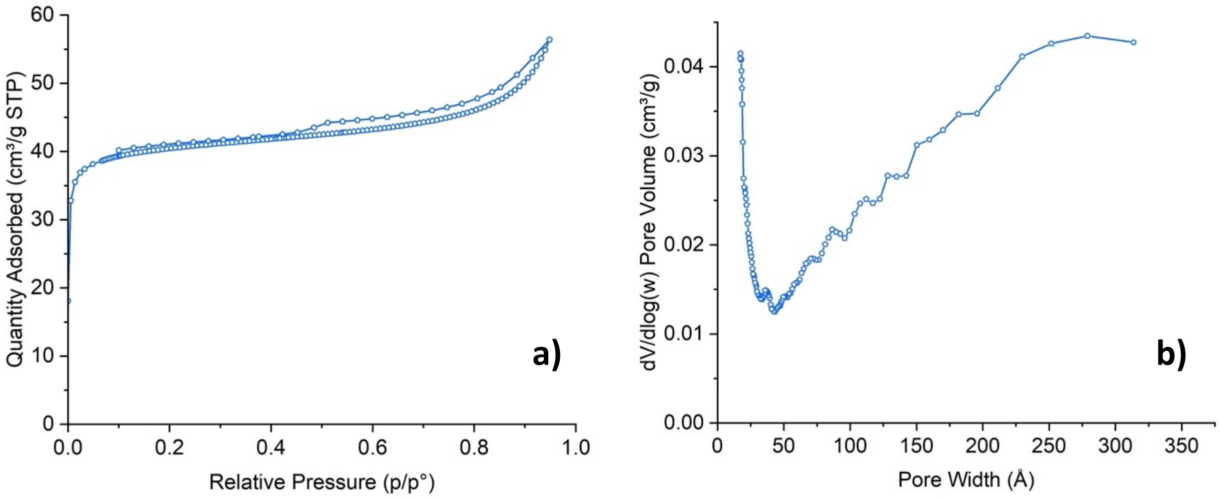

Fig. S3 a) N_2 physisorption isotherm of SAPO-11(2.7) demonstrating a type IV isotherm which is common for SAPO-11. **b)** BJH pore size distribution plot of SAPO-11(2.7) showing that the hysteresis loop observed in Fig. 3a is not caused by ordered mesopores.

Table S3 Surface area and pore volumes of SAPO-11(2.7) confirming that the surface area is in the expected range for SAPO-11.

BET Surface Area (m^2/g)	Micropore Surface Area (m^2/g)	Total Pore Volume (cm^3/g)	Micropore Volume (cm^3/g)
124	97	0.09	0.05

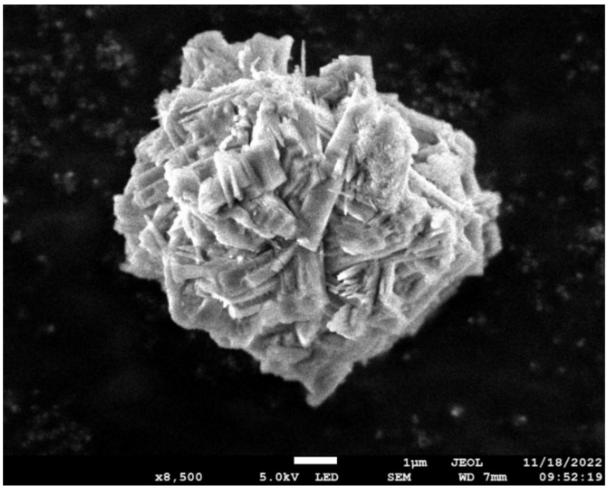

Fig. S4 SEM image of SAPO-11(2.7) demonstrating the expected spherical morphology of SAPO-11.

7.2 SAPO-11 catalysts with different silicon loading

Table S4 Elemental composition of SAPO-11 catalysts with different silicon loadings. Values in bracket indicate the actual Si loading (wt%) of the SAPO-11. catalyst.

Catalyst	Aluminium (wt%)	Phosphorous (wt%)	Silicon (wt%)
SAPO-11(1.1)	23.2 ± 0.5	24.1 ± 0.8	1.1 ± 0.1
SAPO-11(1.4)	23.3 ± 0.2	24.1 ± 0.3	1.4 ± 0.1
SAPO-11(1.7)	24.0 ± 0.3	23.5 ± 0.5	1.7 ± 0.1
SAPO-11(2.0)	23.6 ± 0.3	22.6 ± 0.3	2.0 ± 0.1

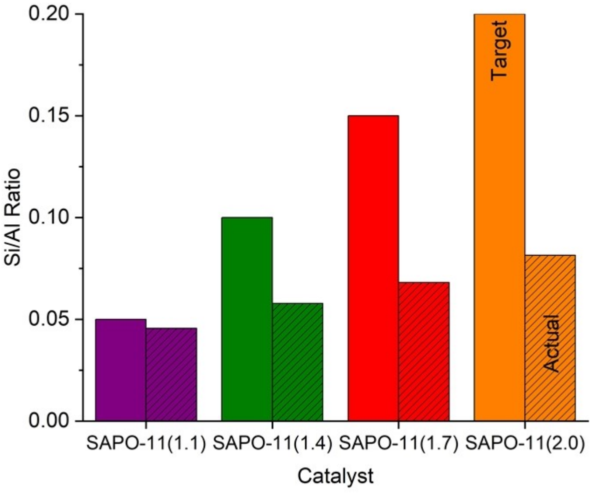

Fig. S5 Target vs actual Si/Al ratios of SAPO-11 catalyst with different Si loading demonstrating the difficulty of substituting Si into the AEL framework.

In line with a previously reported finding,[24] Fig. S5 demonstrates the difficulty in doping silicon into the AlPO-11 framework, with an increasing divergence being observed between target Si/Al gel ratio (0.05-0.20) and actual Si/Al ratio (0.05-0.08) of the solid product as the silicon content of the initial gel is increased. The four SAPO-11 catalysts were phase pure as their respective XRD patterns matched the simulated AEL pattern (Fig. S6).[3] Silicon loading did not affect neither the observed XRD pattern nor the unit cell parameters (Table S5) which are within error tolerance to each other, and consistent with the idealised AEL unit cell lattice.[3] Varying silicon loading did not appear to influence the particle size either (~17 µm, Table S6) as no statistically significant difference was observed. All catalysts had spherical particles (Fig. S7) composed of smaller crystallites which is expected for SAPO-11.[18,20,22,23] A primary peak was observed between -93 and -95 ppm in the ^{29}Si ssNMR spectra (Fig. S8) which can be assigned to Si(3Al, 1Si) species, and a secondary peak was observed at -108 ppm which can be attributed to Si(4Si) species.[20,22,24] There were no significant differences between the spectra of the four catalysts suggesting that silicon speciation is unaffected by silicon loading at the loadings investigated. The ^{29}Si ssNMR spectra confirms that all catalysts possess silicon islands and Brønsted acidic silicon species on the periphery of these silicon islands. The ^{27}Al ssNMR spectra (Fig. S9a) demonstrates a singular peak at 37 ppm for all catalysts which can be attributed to tetrahedral framework $Al(OP)_4$, with no additional peaks confirming the lack of undesirable penta-coordinated, octahedral or hydrated aluminium species.[5,20,23,25,26] Increasing silicon loading does not affect the peak position, and hence aluminium speciation, but does decrease the mass-normalised $Al(OP)_4$ peak intensity. A singular peak at -31 ppm is observed in the ^{31}P ssNMR spectra (Fig. S9b) of all catalysts which is consistent with framework $P(OAl)_4$ species,[5,23,25,26] and lack of extra peaks again confirms no additional phosphorous species. The peak position of the signal once more appears to be unaffected by silicon loading, but in contrast to the $Al(OP)_4$ peak, the mass-normalised $P(OAl)_4$ peak intensity increases in line with loading. The type of porosity present within the SAPO-11 catalysts appears not to be influenced by silicon loading as a type IV N_2 physisorption isotherm (Fig. S10a) is observed for all samples.[19] The pore size distribution plot (Fig. S10b) confirms a lack of ordered mesopores within the frameworks as expected. The total surface area (155-215 m^2g^{-1}) and pore volume (0.10-0.15 cm^3g^{-1}) does however increase (Table S7) with loading and this relationship has also been observed by other authors.[2,22] As expected and desired, increasing silicon loading increases the total number of acid sites present within the SAPO-11 catalyst (Fig. S11) and this is in line with findings reported by Grenev *et al.* [2] The maxima of the NH_3-TPD trace (Fig. S11) is at similar temperatures (~350°C) for the four SAPO-11 catalysts suggesting that silicon loading does not impact the acid strength, and this can be explained by the fact that the four catalyst have similar silicon speciation as indicated by the ^{29}Si ssNMR spectra (Fig. S8). The peak position is consistent with medium strength acid sites as expected for SAPO-11.[23,24,27–29]

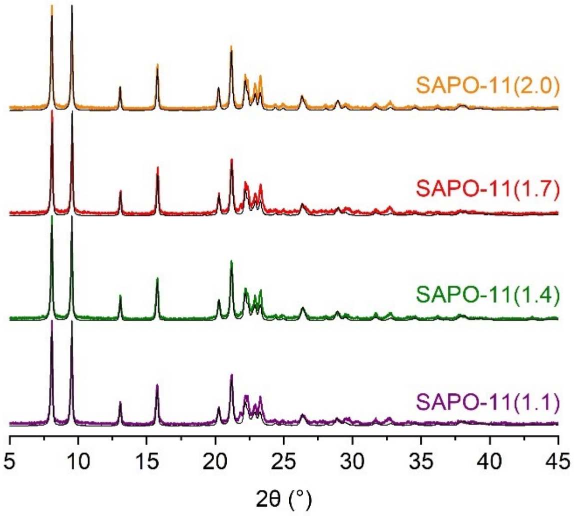

Fig. S6 Powder XRD patterns of dried SAPO-11(1.1-2.0) catalysts (coloured) and calculated AEL pattern (black) demonstrating phase purity.

Table S5 Unit cell parameters obtained via WPPF of SAPO-11 catalysts with different Si loadings showing no influence of Si loading. Error in lattice parameter estimation is ± 0.03 Å.

Catalyst	a (Å)	b (Å)	c (Å)	α (°)	β (°)	γ (°)	Volume (Å^3)
Ideal AEL	8.31	18.73	13.39	90.00	90.00	90.00	2085
SAPO-11(1.1)	8.38	18.53	13.54	90.00	90.00	90.00	2104
SAPO-11(1.4)	8.39	18.52	13.53	90.00	90.00	90.00	2102
SAPO-11(1.7)	8.39	18.51	13.54	90.00	90.00	90.00	2102
SAPO-11(2.0)	8.39	18.50	13.54	90.00	90.00	90.00	2100

Table S6 Average particle size indicating that Si loading has no statistically significant impact on SAPO-11 particle size. Results based on a measurement of 40 particles.

Catalyst	Particle Size (µm)
SAPO-11(1.1)	15 ± 6
SAPO-11(1.4)	16 ± 6
SAPO-11(1.7)	18 ± 6
SAPO-11(2.0)	17 ± 6

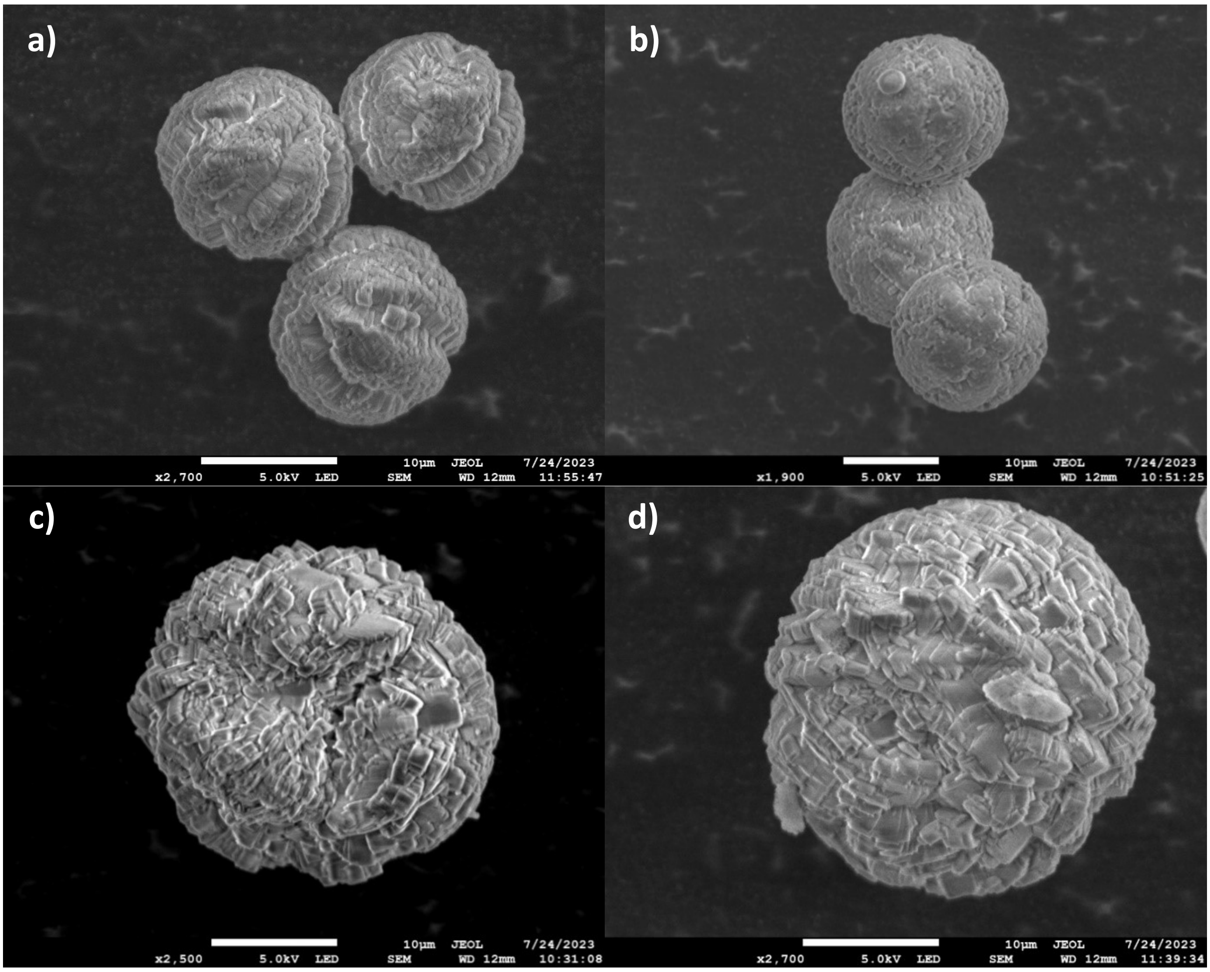

Fig. S7 SEM images of **a)** SAPO-11(1.1) **b)** SAPO-11(1.4) **c)** SAPO-11(1.7) and **d)** SAPO-11(2.0) indicating that Si loading has no impact on SAPO-11 morphology.

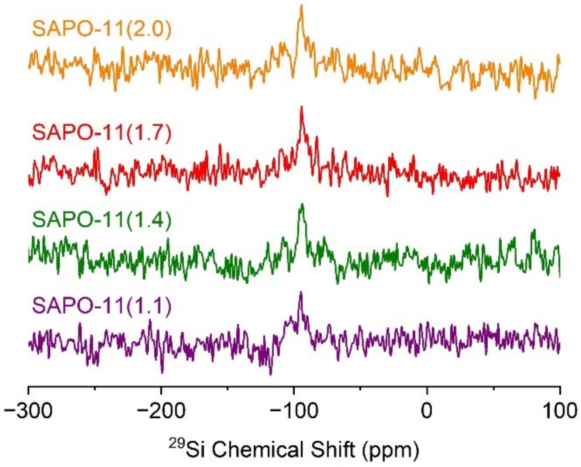

Fig. S8 ^{29}Si ssNMR spectra of SAPO-11(1.1-2.0) catalysts showing that Si loading has no influence on Si speciation.

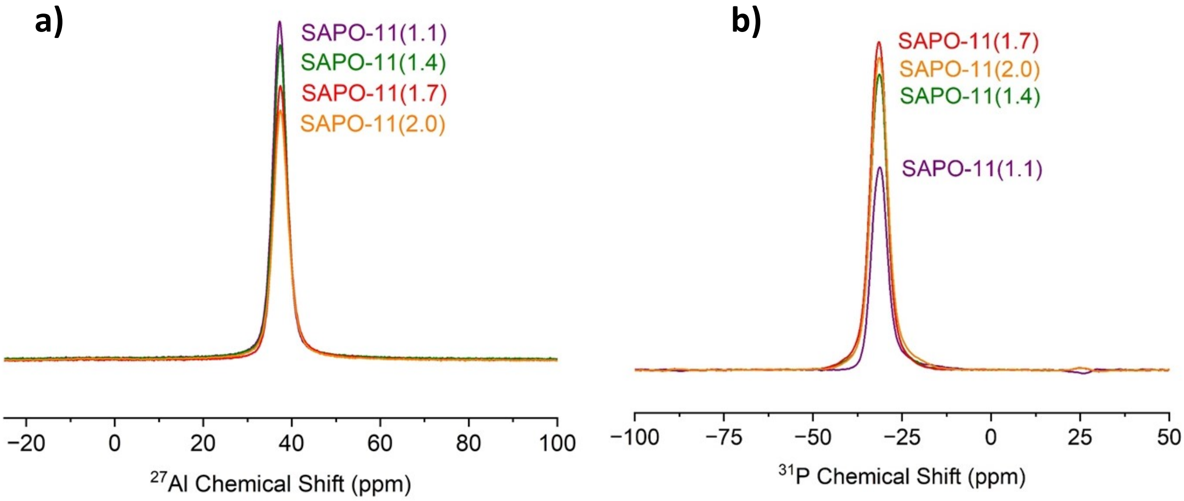

Fig. S9 ssNMR spectra of SAPO-11 catalysts showing that Si loading has no impact on the speciation of **a)** Al or **b)** P in the AEL framework.

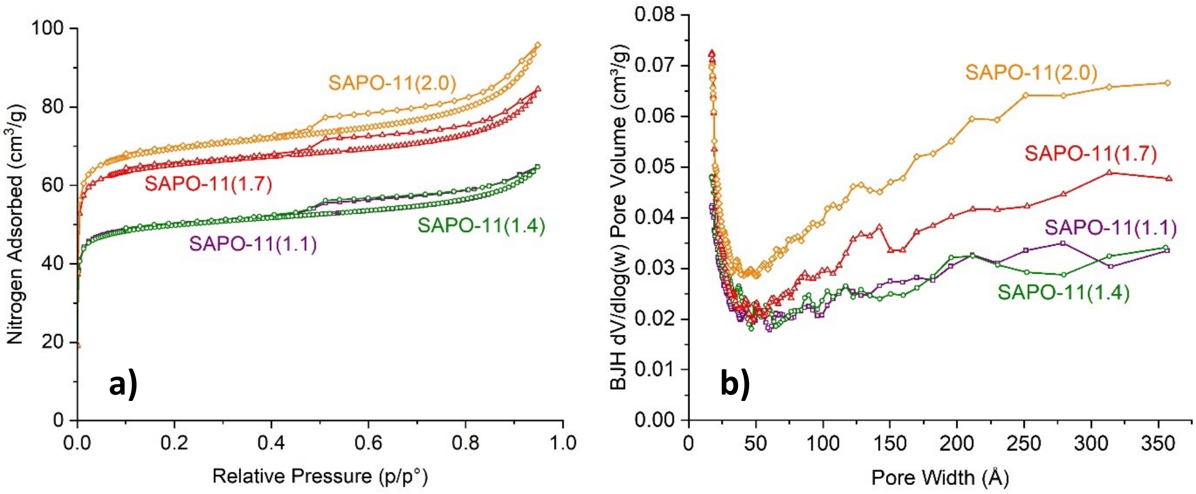

Fig. S10 a) N_2 physisorption isotherm and **b)** BJH pore size distribution of SAPO-11(1.1-2.0) catalysts showing an increase in surface area and pore volume with Si loading.

Catalyst	BET Surface Area (m^2/g)	Micropore Surface Area (m^2/g)	Total Pore Volume (cm^3/g)	Micropore Volume (cm^3/g)
SAPO-11(1.1)	155	124	0.10	0.06
SAPO-11(1.4)	154	121	0.10	0.06
SAPO-11(1.7)	200	158	0.13	0.08
SAPO-11(2.0)	215	166	0.15	0.08

Table S7 Surface area and pore volumes of SAPO-11 catalysts with different Si loadings showing the increase in porosity with Si loading.

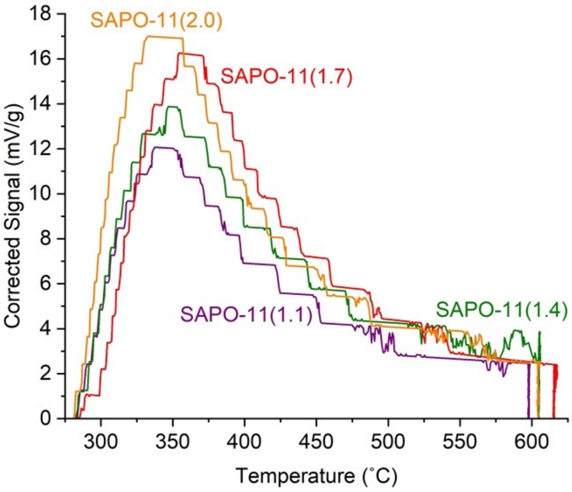

Fig. S11 NH$_3$-TPD spectra of SAPO-11(1.1-2.0) catalysts, demonstrating an increase in number of acid sites with Si loading.

8 Catalytic results

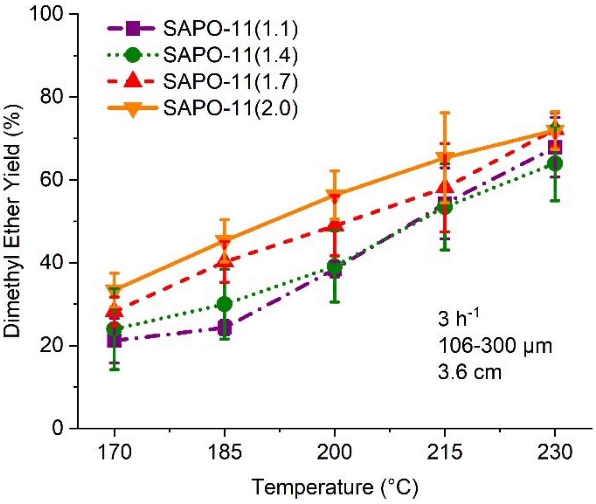

Fig. S12 Influence of Si loading of SAPO-11 on catalytic performance.

Table S8 Influence of Si loading on the deactivation of SAPO-11 catalysts used for methanol dehydration. The relationship between Si loading of SAPO-11 and deactivation is unclear.

Catalyst	Fresh Catalyst Carbon Content (wt%)	Spent Catalyst Carbon Content (wt%)	Carbon Gained (wt%)
SAPO-11(1.1)	0.05 ± 0.01	1.03 ± 0.06	0.98
SAPO-11(1.4)	0.04 ± 0.01	1.21 ± 0.00	1.17
SAPO-11(1.7)	0.03 ± 0.1	1.08 ± 0.01	1.05
SAPO-11(2.0)	0.03 ± 0.01	1.05 ± 0.06	1.02

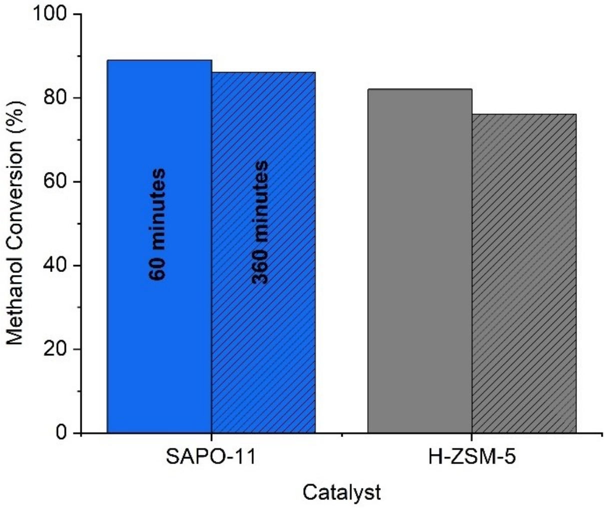

Fig. S13 Comparison of time-on-stream stability of SAPO-11 and H-ZSM-5, demonstrating that over the course of 6 hours' on-stream, SAPO-11 display a smaller decrease in methanol conversion compared to the industrially-relevant H-ZSM-5.

9 Computational modelling of methanol dehydration over large scale SAPO-11(2.7)

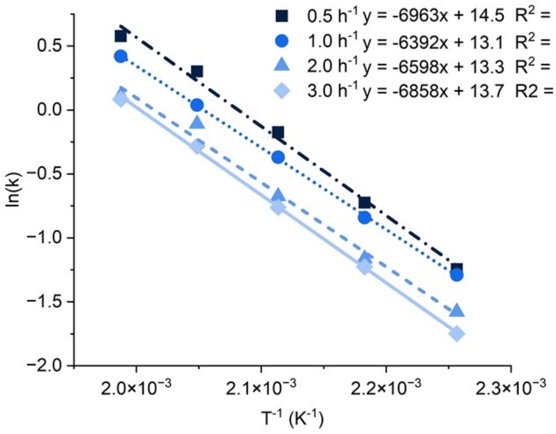

Fig. S14 Arrhenius plot obtained for methanol dehydration over large scale SAPO-11(2.7) catalyst at different methanol weight hourly space velocities. Lack of curvature observed indicates the reaction is in the kinetic and not diffusion-limited regime.

Table S9 Influence of methanol weight hourly space velocity on the calculated activation energy (E_a) and pre-exponential factor (A).

Methanol WHSV (h^{-1})	*Ea (kJ mol^{-1})*	*A (s^{-1})*
0.5	57.9	1.97×10^6
1	53.1	5.03×10^5
2	54.9	5.92×10^5
3	57.0	9.25×10^5
Average	55.7	9.97×10^5

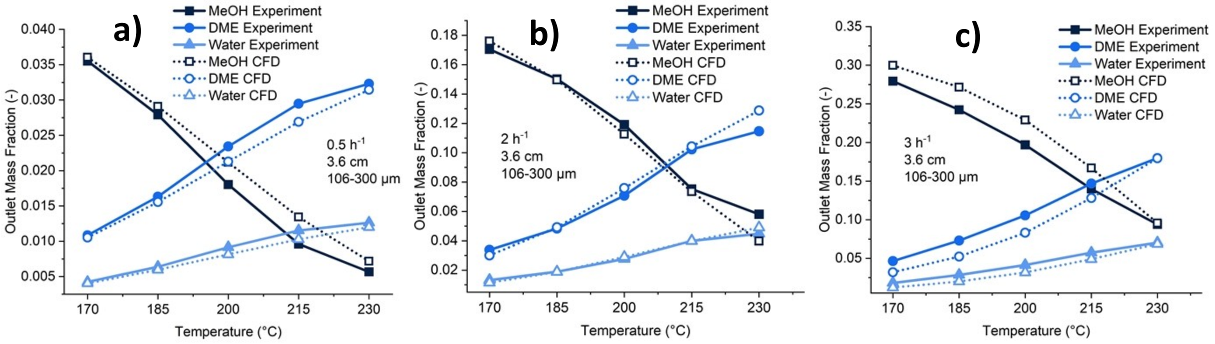

Fig. S15 Comparison between experimental SAPO-11(2.7) and CFD-predicted outlet mass fractions at a range of temperatures at methanol weight hourly space velocities of **a)** 0.5 **b)** 2 and **c)** 3 h^{-1} demonstrating good agreement between experiments and CFD.

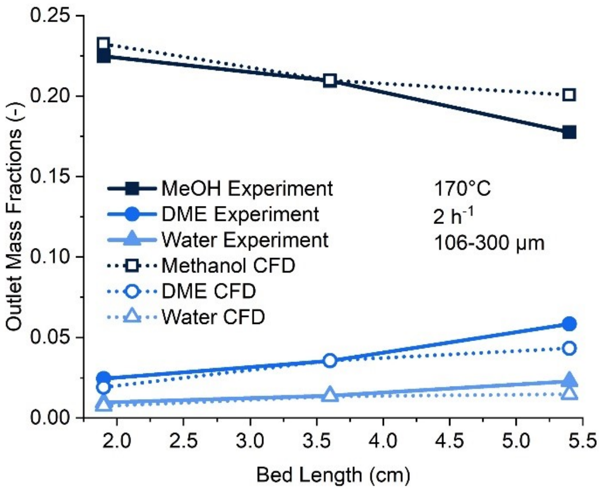

Fig. S16 Comparison between experimental SAPO-11(2.7) and CFD-predicted outlet mass fractions at a range of bed lengths at a temperatures of 170°C demonstrating good agreement between experiments and CFD.

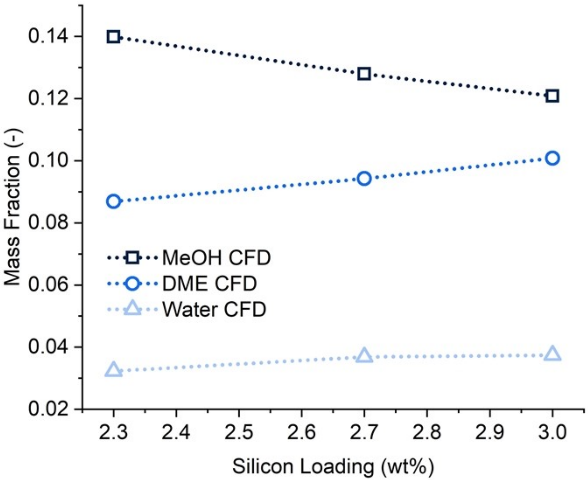

Fig. S17 Influence of silicon loading of SAPO-11 on the CFD-predicted mass fraction during a simulated methanol dehydration reaction. Temperature of 200°C, methanol WHSV of 2 h^{-1}, bed length of 3.6 cm.

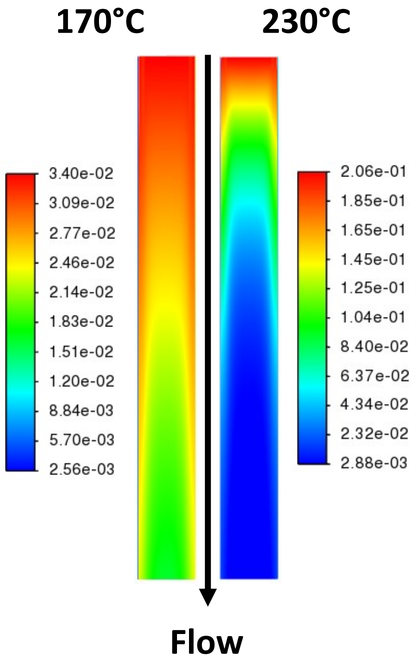

Fig. S18 Two-dimensional contour plots obtained using CFD showing production of DME at two different temperatures at a methanol WHSV of 0.5 h^{-1}. The values are kg m^{-3} s^{-1}. Catalyst bed length of 3.6 cm.

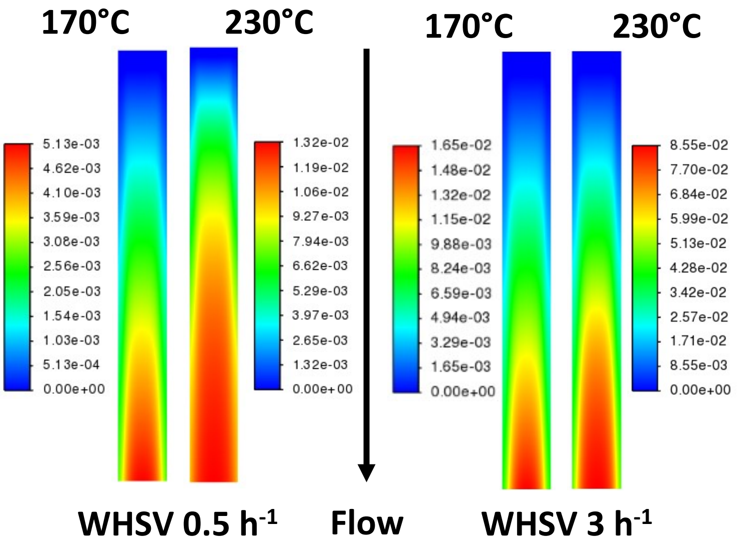

Fig. S19 Two-dimensional contour plots obtained using CFD showing the different distribution of water inside the SAPO-11(2.7) catalyst bed at two different temperatures and methanol WHSVs. The values are the dimensionless mass fractions of water. Catalyst bed length of 3.6 cm.

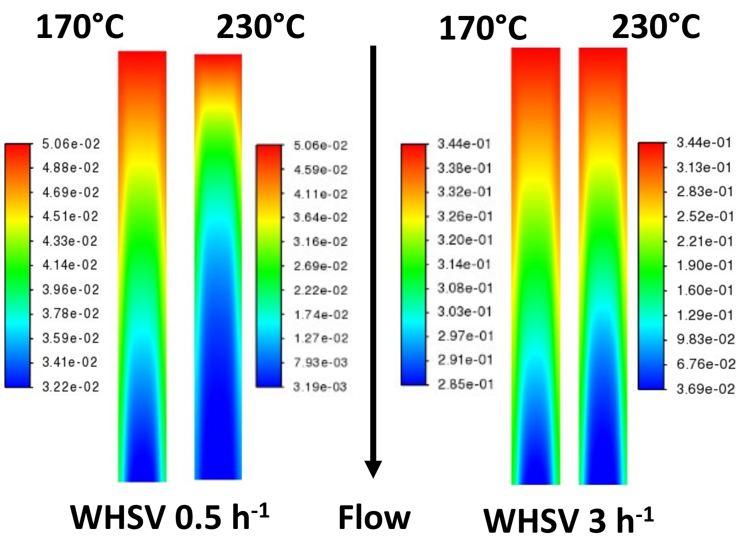

Fig. S20 Two-dimensional contour plots obtained using CFD showing the different distribution of methanol inside the SAPO-11(2.7) catalyst bed at two different temperatures and methanol WHSVs. The values are the dimensionless mass fractions of methanol. Catalyst bed length of 3.6 cm.

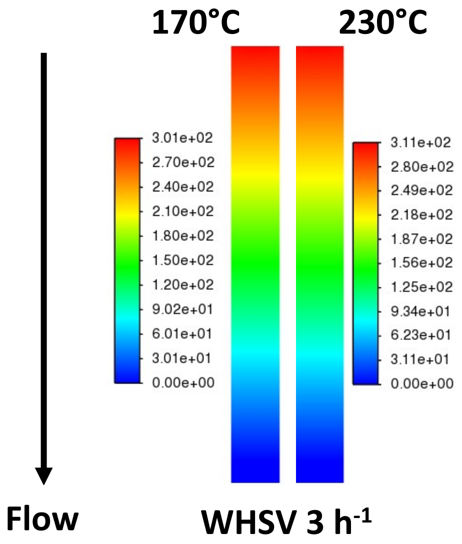

Fig. S21 Two-dimensional contour plots showing the static pressure inside the SAPO-11(2.7) catalyst bed at two different temperatures. The units of static pressure are Pascals. Catalyst bed length of 3.6 cm.

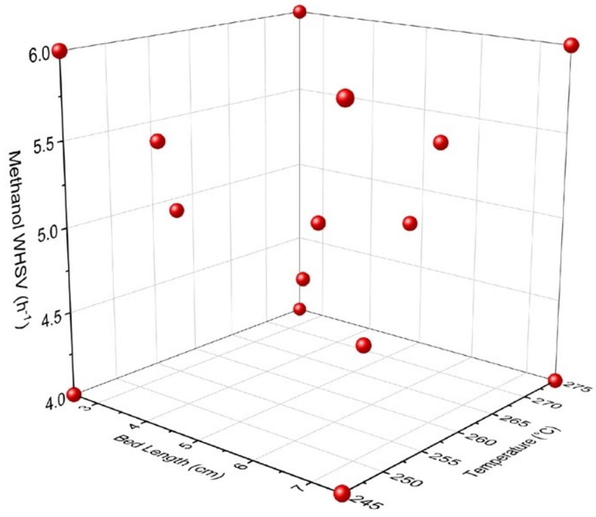

Fig. S22 Experiments conducted to understand the influence of reaction parameters on DME yields and the importance of each variable.

Table S10 Correlation matrix between reaction variables and methanol conversion.

	Bed Length	Temperature	Methanol WHSV	Conversion
Bed Length	1.00	0.07	-0.01	**0.67**
Temperature	0.07	1.00	-0.02	**0.59**
Methanol WHSV	-0.01	-0.02	1.00	**-0.22**
Conversion	**0.67**	**0.59**	**-0.22**	1.00

10 References

1 K. V. V. S. B. S. R. Murthy, S. J. Kulkarni and S. K. Masthan, *Microporous Mesoporous Mater.*, 2001, **43**, 201–209.

2 I. V. Grenev, N. D. Klimkin, I. A. Shamanaeva, A. A. Shubin, I. A. Chetyrin and V. Y. Gavrilov, *Microporous Mesoporous Mater.*, **328**, 111503.

3 AEL: Framework Type, https://asia.iza-structure.org/IZA-SC/framework.php?STC=AEL, (accessed 17 December 2021).

4 M. E. Potter, L. M. Armstrong and R. Raja, *Catal. Sci. Technol.*, 2018, **8**, 6163–6172.

5 M. E. Potter, J. Amsler, L. Spiske, P. N. Plessow, T. Asare, M. Carravetta, R. Raja, P. A. Cox, F. Studt and L. M. Armstrong, *ACS Catal.*, 2023, **13**, 5955–5968.

6 M. E. Potter, M. E. Cholerton, J. Kezina, R. Bounds, M. Carravetta, M. Manzoli, E. Gianotti, M. Lefenfeld and R. Raja, *ACS Catal.*, 2014, **4**, 4161–4169.

7 S. Hoops, R. Gauges, C. Lee, J. Pahle, N. Simus, M. Singhal, L. Xu, P. Mendes and U. Kummer, *Bioinformatics*, 2006, **22**, 3067–3074.

8 Z. Michalewicz, *Genetic Algorithms + Data Structures = Evolution Programs*, Springer Berlin Heidelberg, 1996.

9 D. W. Marquardt, *Journal of the Society for Industrial and Applied Mathematics*, 1963, **11**, 431–441.

10 K. Levenberg and F. Arsenal, *Q. Appl. Math*, 1944, **2**, 164–168.

11 Ansys Fluent, http://www.ansys.com/, (accessed 19 November 2024).

12 S. V Patankar and D. B. Spalding, *Int. J. Heat. Mass. Transf.*, 1972, **15**, 1787–1806.

13 S. Kyrimis, M. E. Potter, R. Raja and L. M. Armstrong, *Faraday Discuss.*, 2021, **230**, 100–123.

14 S. Ergun, *Chem. Eng. Prog.*, 1952, **48**, 89–94.

15 A. De Klerk, *AIChE Journal*, 2003, **49**, 2022–2029.

16 S. Kyrimis, R. Raja and L. M. Armstrong, *Fuel*, 2024, **368**, 131511.

17 Sartorius MODDE, https://www.sartorius.com/en/products/process-analytical-technology/data-analytics-software/doe-software/modde, (accessed 19 November 2024).

18 Z. Chen, X. Li, Y. Xu, Y. Dong, W. Lai, W. Fang and X. Yi, *Catal. Commun.*, 2018, **103**, 1–4.

19 M. Thommes, K. Kaneko, A. V. Neimark, J. P. Olivier, F. Rodriguez-Reinoso, J. Rouquerol and K. S. W. Sing, *Pure Appl. Chem.*, 2015, **87**, 1051–1069.

20 A. K. Sinha and S. Seelan, *Appl. Catal. A Gen.*, 2004, **270**, 245–252.

21 M. Sánchez-Contador, A. Ateka, A. T. Aguayo and J. Bilbao, *J. Ind. Eng. Chem.*, 2018, **63**, 245–254.

22 P. Liu, J. Ren and Y. Sun, *Microporous Mesoporous Mater.*, 2008, **114**, 365–372.

23 P. Mériaudeau, V. A. Tuan, V. T. Nghiem, S. Y. Lai, L. N. Hung and C. Naccache, *J. Catal.*, 1997, **169**, 55–66.

24 M. R. Agliullin, Y. G. Kolyagin, D. V. Serebrennikov, N. G. Grigor’eva, A. S. Dmitrenok, V. N. Maistrenko, E. Dib, S. Mintova and B. I. Kutepov, *Microporous Mesoporous Mater.*, 2022, **338**, 111962.

25 A. M. Prakash, S. V. V. Chilukuri, R. P. Bagwe, S. Ashtekar and D. K. Chakrabarty, *Microporous Mater.*, 1996, **6**, 89–97.

26 M. E. Potter, J. Kezina, R. Bounds, M. Carravetta, T. M. Mezza and R. Raja, *Catal. Sci. Technol.*, 2018, **8**, 5155.

27 W. Dai, W. Kong, G. Wu, N. Li, L. Li and N. Guan, *Catal. Commun.*, 2011, **12**, 535–538.

28 R. B. Borade and A. Clearfield, *J. Mol. Catal.*, 1994, **88**, 249–265.

29 K. S. Yoo, J. H. Kim, M. J. Park, S. J. Kim, O. S. Joo and K. D. Jung, *Appl. Catal. A Gen.*, 2007, **330**, 57–62.